DOI: 10.1021/cg100560s

CRYSTAL GROWTH & DESIGN Article

2010, Vol. 10
3983–3989

Facile Chemical Synthesis of Nanocrystalline Thermoelectric Alloys Based on Bi−Sb−Te−Se

Anuja Datta,[†] Jagannath Paul,[†] Arik Kar,[‡] Amitava Patra,[‡] Zhengliang Sun,[§] Lidong Chen,[§] Joshua Martin,[#] and George S. Nolas*,[†]

[†]*Department of Physics, University of South Florida, Tampa, Florida 33620,* [‡]*Department of Materials Science, Indian Association for the Cultivation of Science, Kolkata 700032, India,* [§]*State Key Laboratory of High Performance Ceramics and Superfine Microstructures, Shanghai Institute of Ceramics, Chinese Academy of Sciences, Shanghai 200050, China, and* [#]*Ceramics Division, National Institute of Standards and Technology (NIST), Gaithersburg, Maryland 20899*

Received April 27, 2010; Revised Manuscript Received July 14, 2010

ABSTRACT: High yield syntheses of size-confined Bi_2Te_3 and Sb_2Te_3 nanocrystals and nanoflakes, and their alloys, were carried out by a facile glycol-mediated solvothermal process. Phase purity and good crystalline quality were achieved for all alloy compositions by this synthesis process. The isotropically and anisotropically shaped nanocrystals were obtained without using any capping molecule, template, or ligand. Plausible growth mechanisms have been proposed. Densification via spark plasma sintering allowed for dense bulk polycrystalline specimens with nonagglomerated nanograins. This work is of interest in the context of research toward enhancing the thermoelectric properties of these materials. The synthesis process may be modified and extended to design nanostructures of thermoelectric materials with related crystal structures.

1. Introduction

Research in the field of thermoelectrics has experienced an upsurge over the past decade due to the growing interest in nanomaterials.[1−5] The specific material property requirements for thermoelectric materials can be quantified by the dimensionless figure of merit, $ZT = S^2\sigma T/\kappa$, where S is the Seebeck coefficient, σ is the electrical conductivity, T is the absolute temperature, and κ is the thermal conductivity ($\kappa = \kappa_L + \kappa_e$, the lattice and electronic contributions, respectively).[6] Nanoscale effects have so far been established as a means of enhancing ZT in thermoelectric materials as evidenced by both experimental and theoretical reports on superlattice structures and bulk materials with nanoscale domains.[5,7−13] Enhancement in ZT in materials that contain nanoscale domains has been reported to be due to an increased density of states near the Fermi level[1,3,14] as well as enhanced interfacial phonon scattering and charge carrier filtering.[1,3−5,7−9] Despite these recent results, limitations in applicability of this technology exist for these materials, partly because of the difficulties with scalability and cost.

The traditional state of the art thermoelectric cooling material are alloys of bismuth telluride (Bi_2Te_3), a material that is well studied and also commercially available in small-scale refrigerators.[6] However, the maximum room temperature ZT value in these devices has thus far been limited to $ZT \sim 1$. This value is too low for thermoelectrics to become competitive with conventional compressor-based refrigerators. The best materials for thermoelectric cooling applications have a ternary composition $Bi_{2-x}Sb_xTe_3$ ($x = 0-2$) and are doped with Se. These materials are typically prepared from a complete solid solubility among the three compounds Bi_2Te_3, Sb_2Te_3, and Bi_2Se_3.[6,15] Yim and Rosi[16] reported that a large variation in this alloy composition is possible without greatly affecting ZT, provided precise doping is maintained. Solid solution alloying between the isostructural $Bi_2Te_3-Sb_2Te_3$ and $Bi_2Te_3-Bi_2Se_3$ phases results in a significant decrease in κ at the "alloy limit". This type of alloying has therefore always been a target region for these thermoelectric materials.

The crystal structures of these alloys show anisotropy originating from the rhombohedral structure composed of quintuple atomic layer series along the c-axis.[17] To date the most successful methods in synthesizing these materials are crystals grown from the melt.[6,18] On the basis of recent reports on the perspectives of nanostructured alloys for thermoelectric applications, there have been persistent efforts to prepare Bi_2Te_3 based alloy materials in polycrystalline form with nanograins.[13,19−25] Over the past few years, reports have been published indicating enhanced thermoelectric properties of nanostructured bismuth antimony telluride alloys prepared by ball milling of elemental chunks followed by hot pressing,[19−21] by controlled electrodeposition,[22,23] and through melt spinning.[24] Only recently have chemical synthesis attempts of bismuth antimony telluride alloy nanocrystals been investigated. These include an acid pyrolysis process,[25] microemulsion process,[26] organometallic colloidal synthesis routes,[13,27−31] soft template assisted hydrothermal/solvothermal routes,[32−37] and microwave-assisted synthesis process.[38] Nevertheless, a more simple and scalable chemical process using less toxic and less expensive chemicals would be most desirable. Herein we build on and further develop the bottom-up approach we first employed in PbTe nanocomposites[7,8] and report on a high yield and readily scalable glycol based approach for the synthesis of nanocomposites of alloy compositions in the $Bi_{2-x}Sb_xTe_{3-y}Se_y$ ($x = 0$, 1.5, 2 when $y = 0$, 0.1, 0.2) system. No complex organic ligands or templating molecules have been used in our synthesis process to control the crystal size. This simplified reaction process effectively produced small nanocrystals of different shapes with at least one dimension in the 5−18 nm range. We achieved phase

*To whom correspondence should be addressed. E-mail: gnolas@usf.edu.

Published on Web 08/02/2010

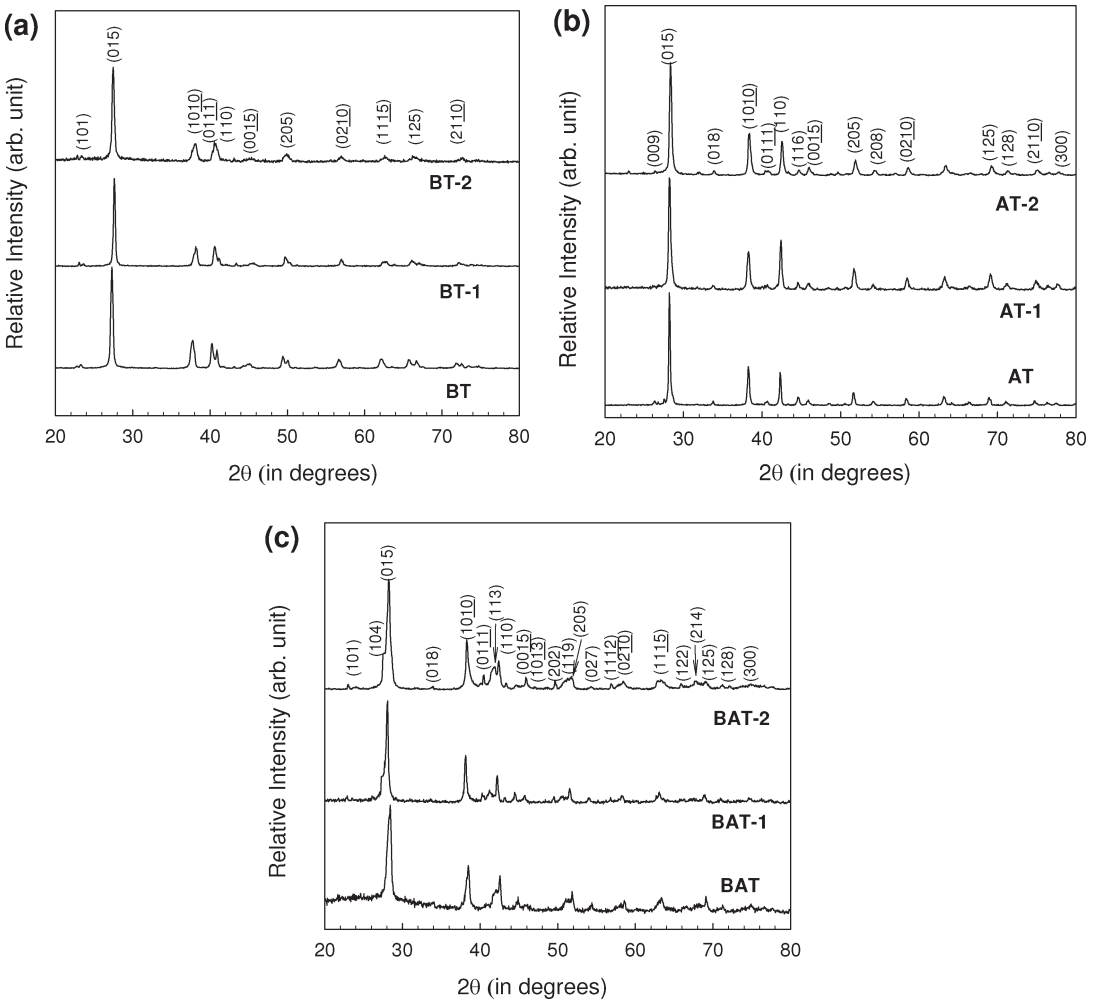

Figure 1. XRD spectra of the undoped and Se doped (a) Bi_2Te_3 nanocrystals (BT, BT-1, and BT-2 refer to undoped and Se doping with nominal Te:Se ratios of 2.9:0.1 and 2.8:0.2, respectively). (b) Sb_2Te_3 nanoflakes (AT, AT-1, and AT-2 refer to undoped, and Se doping with nominal Te:Se ratios of 2.9:0.1 and 2.8:0.2, respectively) and (c) $Bi_{0.5}Sb_{1.5}Te_3$ nanocrystals (BAT, BAT-1, and BAT-2 refer to undoped and Se doping with nominal Te:Se ratios of 2.9:0.1 and 2.8:0.2, respectively.

purity for all specimens within the resolution limits of X-ray diffraction (XRD). Densification of the nanocrystals into bulk polycrystalline pellets was achieved via spark plasma sintering (SPS) allowing for Hall measurements on dense polycrystalline specimens.

2. Experimental Section

Bismuth telluride and antimony telluride based undoped and Se doped nanocrystals were prepared by a ethylene glycol-mediated solvothermal process. For the synthesis, bismuth nitrate ($Bi(NO_3)_3 \cdot 5H_2O$), antimony(III) chloride ($SbCl_3$), and selenium dioxide (SeO_2) were chosen as the Bi, Sb, and Se sources, respectively. Sodium tellurite (Na_2TeO_3) was the tellurium source for all the syntheses. Hydrazine monohydrate ($N_2H_4 \cdot H_2O$) was used as a reducing agent. All the chemicals were of analytical grade and were used without further purification.

Initially, 2 mmol of bismuth nitrate was dissolved in 20 mL of ethylene glycol with the help of 2 mL of glacial acetic acid for synthesizing Bi_2Te_3 nanocrystals. When completely dissolved, a molar proportion of sodium tellurite (3 mmol) was added to the bismuth nitrate solution and stirred for 30 min for homogeneity. Hydrazine monohydrate (15 mL) was then quickly added to the solution to make a volume of 40 mL (80% of the volume of the container) and the entire mixture was sealed within a custom built 50 mL Teflon container. After sealing, the reactant filled Teflon container was inserted into a stainless steel chamber. The stainless steel cap was tightly screwed to avoid solvent loss at temperature. The vessel was then kept at 230 °C for 12 h. All reactions were carried out at this specified temperature and time. To synthesize Sb_2Te_3 nanocrystals, the same procedure was followed except bismuth nitrate was replaced with an equal molar quantity of antimony chloride without adding acetic acid. In order to dope with Se, SeO_2 was dissolved together with appropriate concentrations of $Bi(NO_3)_3 \cdot 5H_2O$ (for Bi_2Te_3) or $SbCl_3$ (for Sb_2Te_3), followed by the addition of sodium tellurite and hydrazine monohydrate in succession.

In addition to the binary tellurides, undoped and Se doped ternary $Bi_{0.5}Sb_{1.5}Te_3$ nanocrystals were also synthesized using the identical process with similar cation and anion sources and reductant. In this synthesis procedure, 0.5 mmol of bismuth nitrate was first dissolved in 20 mL of ethylene glycol with 2 mL of glacial acetic acid. After completely dissolving, 1.5 mmol of antimony chloride was added and stirred until dissolved. It was followed by the addition of the required sodium tellurite and hydrazine monohydrate, and heating for 12 h at 230 °C in our custom built container. Selenium doping was achieved for all nanocrystals by varying the Te:Se ratios, as described above.

After each reaction, the container was slowly air cooled to room temperature. The products were recovered after centrifuging and washing several times with distilled water and dehydrated ethyl alcohol to remove any unreacted chemicals as well as to clean the solvent residue from the surface of the nanocrystals. Yields of more than 1 g per batch were readily achieved. The products were vacuum-dried at room temperature and collected for powder X-ray diffraction (XRD, Bruker AXS D8, Lynx Eye Position sensitive detector), energy dispersive X-ray spectroscopy (EDS, Oxford Instruments

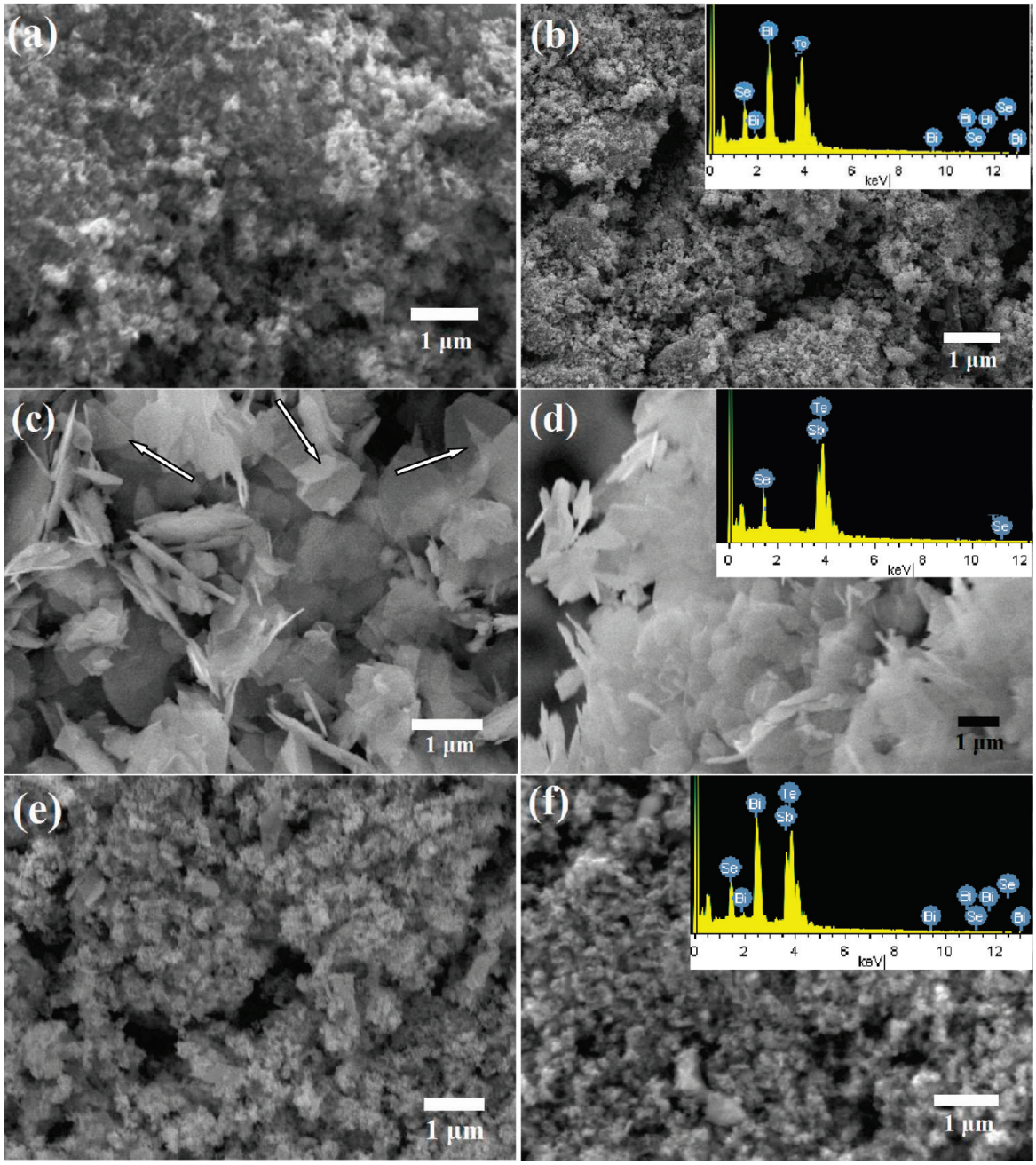

Figure 2. SEM images of the undoped and Se doped (Te/Se ratio of 2.8:0.2) nanocrystals of Bi_2Te_3 (a and b), Sb_2Te_3 nanoflakes (c and d), and $Bi_{0.5}Sb_{1.5}Te_3$ (e and f). Corresponding EDS spectra of the doped specimens are shown as the inset images.

INCAX sight), scanning electron microscopy (SEM, JEOL JSM 6390 LV), and transmission electron microscopy (TEM, JEOL 2100) analyses.

Henceforth, undoped and Se doped Bi_2Te_3 and Sb_2Te_3 specimens will be referred to as BT, BT-1, and BT-2 and AT, AT-1, and AT-2, respectively and undoped and Se doped $Bi_{0.5}Sb_{1.5}Te_3$ will be referred to as BAT, BAT-1, and BAT-2. In all specimens, the numbering 1 and 2 refers to nominal starting Te:Se ratios of 2.9:0.1 and 2.8:0.2, respectively.

3. Results and Discussion

The crystalline phase and purity of the specimens were investigated by powder XRD. Figure 1a−c shows indexed XRD spectra of the undoped and Se doped Bi_2Te_3, Sb_2Te_3, and $Bi_{0.5}Sb_{1.5}Te_3$ specimens, respectively. The relatively large full width at half-maximum in all specimens is indicative of the small crystallite sizes. The Bi_2Te_3 XRD spectra were indexed with rhombohedral symmetry (space group $R\bar{3}m$) and have an average crystallite size of ~20 ± 5 nm as calculated by the Debye−Scherrer equation.[39] The Sb_2Te_3 XRD spectra (Figure 1b) were also indexed with rhombohedral symmetry (space group $R\bar{3}m$). The intense and sharp XRD peaks from the Sb_2Te_3 nanocrystals are typical signatures of a high degree of crystallinity. No detectable impurity peaks were observed. XRD spectra of the $Bi_{0.5}Sb_{1.5}Te_3$ specimens (Figure 1c) were also assigned to the rhombohderal (space group $R\bar{3}m$) lattice structure. The average crystallite size of these specimens was ~18 nm with a size distribution of ±3 nm. Se-doped specimens did not show any Se impurities in the XRD spectra. Hall data on dense polycrystalline specimens confirmed an increase in the carrier concentration with Se doping, validating Se doping of the nanocrystals.

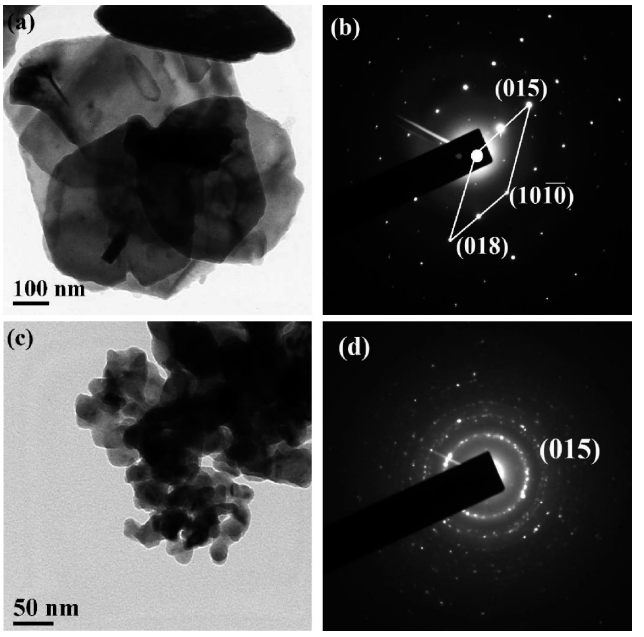

Figure 3. (a) Bright field TEM image of Sb_2Te_3 nanoflakes. Superimposed flakes are very thin and devoid of structural defects. (b) Single crystalline SAED pattern of a Sb_2Te_3 nanoflake. The diffraction spots indexed to the corresponding planes indicates rhombohedral structure. (c) Bi_2Te_3 nanocrystals in aggregate. (d) Polycrystalline SAED pattern of the Bi_2Te_3 nanocrystals. The diffraction ring is indexed to the (015) plane of the rhombohedral Bi_2Te_3.

The morphology and size of the as-synthesized nanocrystals characterized by SEM and TEM are shown in Figures 2a−f and 3a−d, respectively. SEM images of the aggregated BT and BT-2 nanocrystals (Figure 2a,b) indicate the nanocrystals to be spherical in shape. A representative EDS spectrum of BT-2 nanocrystals is shown in the inset of the SEM image (Figure 2b). EDS analyses on each specimen was accomplished by collecting spectra from over 50 different nanocrystals, suggesting a nearly uniform stoichiometry. Elemental mapping also indicated strong homogeneity for all specimens. All the BT specimens were found to have a 0.2 at % lower atomic percentage of Te than their respective nominal values. Specimens AT and AT-2 (Figure 2c,d) are composed of randomly oriented very thin flakes with lengths varying from ~100 nm to 1.5 μm. The image shown in Figure 2c, taken with an accelerating voltage of 20 keV, reveals the fine nanostructure in the Sb_2Te_3 nanoflakes. The very thin nature of the flakes can be observed from the figure, where two back-to-back superimposed nanoflakes are clearly visible (shown by arrows in Figure 2c). This phenomenon suggests that the thickness of the nanoflakes is of the same order as the penetration depth of the secondary electrons emitted from the nanoflake surfaces. Typical thicknesses estimated from the SEM images were ~5−10 nm and represent very thin Sb_2Te_3 nanoflakes compared to other reports prepared by chemical routes.[30,32−34] EDS spectra for the AT-2 specimen confirm Se doping. Unlike Sb_2Te_3, $Bi_{0.5}Sb_{1.5}Te_{3-y}Se_y$ nanocrystals do not appear to show any dimensional heterogeneity (Figure 2e,f). Agglomeration of the nanoparticles of ~18 nm was clearly observed. A typical EDS spectrum representing the composition of the Se doped BAT specimens is shown in the inset of Figure 2f.

The bright field TEM images from the AT and BT specimens, shown in Figure 3a−d are typical for these nanostructures. Clustering of randomly dispersed Sb_2Te_3 nanoflakes are observed in Figure 3a. The observed black bands are the stress-bands generated in the thin flakes during formation. The selected area electron diffraction (SAED) pattern collected from a nanoflake is shown in Figure 3b. The pattern clearly shows the single crystalline nature of the Sb_2Te_3 nanoflakes. The lattice planes indexed in the figure reveals a preferred growth along the [010] direction. Structurally, the SAED pattern resembles the rhombohedral crystal form. The TEM images additionally reveal that the as-obtained Sb_2Te_3 nanoflakes are structurally uniform and free from planar defects. Figure 3c is a TEM image of a cluster of BT nanocrystals with a size distribution of ~15−25 nm. The BT specimens typically clustered in this way. The SAED pattern collected from the randomly oriented cluster of BT nanocrystals resembles that of a polycrystalline specimen (Figure 3d). The diffraction plane (015) is a major diffraction plane from these clustered nanocrystals. Clearly developed rings and bright diffraction spots are indicative of the crystallinity and also suggest the absence of planar structural defects.

The formation of isotropic and anisotropic nanocrystals in ethylene glycol has been investigated by many groups.[40,41] Ethylene glycol as a reaction medium acts as both the solvent and the reducing agent. The polyol solvent, heated above its boiling point in the pressurized solvothermal vessel, has a much higher reducing ability and therefore can easily reduce the metal ion. $Bi(NO_3)_3\cdot 5H_2O$, $SbCl_3$, and Na_2TeO_3 are all soluble in ethylene glycol and can be easily reduced because of their low reduction potentials in this slightly basic medium ($Bi^{3+} + 3e^- \rightarrow Bi^0$ −0.452 V; $Sb^{3+} + 3e^- \rightarrow Sb^0$ −0.639 V; $TeO_3^{2-} \rightarrow Te^{4+} \rightarrow Te^0$ −0.42 V). Te has the highest reduction potential thus the rate of reduction of tellurite to Te is very fast. This is why there is always less Te as compared to the nominal concentration and the nanocrystals of Bi_2Te_3, Sb_2Te_3 and $Bi_{0.5}Sb_{1.5}Te_{3-y}Se_y$ are slightly Te deficient. $N_2H_4\cdot H_2O$ added as the reducing agent also reduces the sodium tellurite in glycol medium as per the reaction,

$$TeO_3^{2-} + 2OH^- \rightarrow Te^0 + 2O_2 + H_2O + 5e^-$$

The $N_2H_4\cdot H_2O$ always maintains an excess reducing environment thereby preventing surface oxidation of the nanocrystals while at the same time inhibiting the precipitation of tellurium compounds. The available Te atoms react readily with the available Bi/Sb or Bi and Sb to form Bi_2Te_3, Sb_2Te_3, and $Bi_{0.5}Sb_{1.5}Te_{3-y}Se_y$ nuclei. The nuclei are then sufficiently fed with more precursor materials thereby forming the nanocrystals. Commonly, $A_2^{V}B_3^{VI}$ alloys have an inherently anisotropic bonding environment which causes faster growth along the top-bottom crystalline planes compared to the *c*-axis thus tending to form a platelet-like morphology.[36,42] This feature, along with the high reactivity of Te with Bi precursors, often requires strong control of the reaction kinetics. Here the use of Na_2TeO_3 as the Te source is a key factor for the controlled growth of the nanocrystals. The TeO_3^{2-} ion is a weak base and releases Te in a fast and steady rate in ethylene glycol medium. Spherical nanocrystals of $Bi_2Te_{3-y}Se_y$ and $Bi_{0.5}Sb_{1.5}Te_{3-y}Se_y$ then form by a seeded growth mechanism, where the controlled rate of dissociation of $Bi(NO_3)_3\cdot 5H_2O$ and the steady supply of Te help the isotropic growth of the nanocrystals. Since no capping agent is used in our nanocrystal syntheses, we presume that ethylene glycol may also form a protective layer around the particle surfaces via an interaction with its OH group and the surface of the precipitate thereby preventing particle growth and agglomeration.

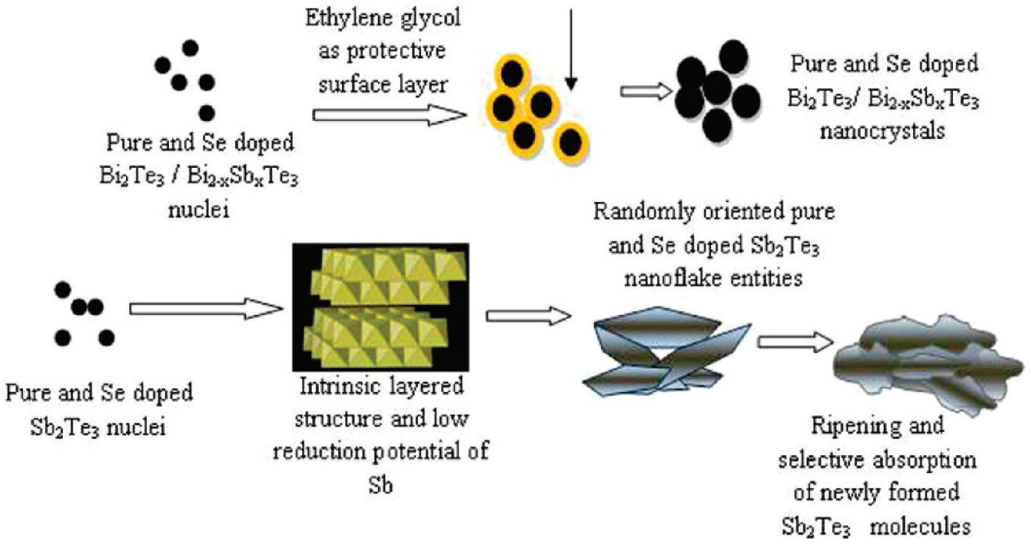

Figure 4. Schematic illustration of the growth process of Bi_2Te_3, Sb_2Te_3, and $Bi_{0.5}Sb_{1.5}Te_3$ nanocrystals with different morphologies.

The formation of irregular hexagonal Sb_2Te_3 nanoflakes may be due to the relatively slower reactivity of Sb with Te in ethylene glycol. This allows the reaction to progress slowly and the inherent anisotropic, layered crystal structure of Sb_2Te_3 is maintained giving rise to the observed flake-like structure. The flakes grow longer because of the selective absorption of the newly generated Sb_2Te_3 molecules at certain faces. With a longer reaction time, the growth of the small flakes is suppressed by the larger ones thus causing a large crystal size distribution.[43] A depiction of the growth mechanism of the nanoparticles and nanoflakes described above is illustrated schematically in Figure 4.

In order to avoid conglomeration that occurs when nanoscale powders are mixed and densified with micrometer-scale powders, we densified solely the nanocrystals employing SPS (Sumitomo Dr. Sinter SPS-2040). Densification of the undoped and Se doped Bi_2Te_3, Sb_2Te_3, and $Bi_{0.5}Sb_{1.5}Te_3$ nanocrystals were carried out at 60 MPa pressure and temperatures of 330, 320, and 305 °C, respectively, for 20 min. The smaller grains in the bulk specimens after SPS, measured from several SEM images, were in the range of 20−100 nm. A representative SEM image of a fractured surface of the BT specimen is shown in Figure 5. The bulk polycrystalline specimens were cut into 0.5 mm × 2 mm × 8 mm parallelepipeds for Hall measurements. Room temperature four-probe Hall measurements were conducted at multiple positive and negative magnetic fields up to 2.5 T to eliminate voltage probe misalignment effects using a Quantum Design PPMS (Physical Property Measurement System, ACT option). The measurement uncertainty is 4%. A linear and negative (positive) magnetic field dependence of the Hall resistance confirms dominant n-type (p-type) conduction for the BT (BAT and AT) specimens. These Hall measurements corroborate the EDS results and indicate that Se doping of nanocrystals can successfully vary the carrier concentration of the bulk composites, as demonstrated for PbTe.[7,8]

The room temperature carrier concentration, n, for the dense (> 95%) bulk Bi_2Te_3 is relatively high ($n = 4.8 \times 10^{19}$ cm^{-3} for BT) and increases with increasing Se doping ($n = 6.6 \times 10^{19}$ cm^{-3} for BT-1 and $n = 8.8 \times 10^{19}$ cm^{-3} for BT-2). Four-probe resistivity, ρ, steady-state Seebeck Coefficient (gradient sweep method), S, and thermal conductivity,

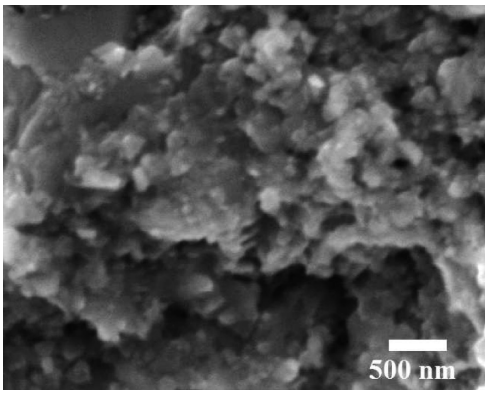

Figure 5. A representative SEM image of the fractured surface of the Bi_2Te_3 nanocomposite pellet BT after SPS densification.

κ, measurements on 2 mm × 2 mm × 5 mm parallelepipeds from 12 to 300 K were conducted in a custom radiation-shielded vacuum probe,[44] with uncertainties of 4, 6, and 8%, respectively, and are shown in Figure 6a−c. The room temperature variation of $|S|$ with n is shown in the inset of Figure 6a. The solid line represents the theoretical bulk relation, assuming a single parabolic band model with ionic impurity scattering[45] as the dominant scattering mechanism at room temperature and considering the integral density of states effective mass $m_d^* = 0.27m_e$,[46] where m_e is the mass of an electron. This plot indicates an enhancement in $|S|$ for the doped polycrystalline bulk nanocomposites over theoretical predictions[45] and bulk polycrystalline specimens.[47,48] As shown in Figure 6b, ρ decreases with increasing Se doping, as expected. The κ measurements show a decrease with Se doping, presumably due to alloy scattering at the Te site (Figure 6c). The maximum in κ is lower for $Bi_2Te_{3-y}Se_y$ as compared to Bi_2Te_3 and is indicative of such alloy scattering. The above TE properties were independent of the direction (parallel and perpendicular to the SPS pressing direction) of measurement. This is due to the random orientation of the grains within the densified specimens. A detailed study of the transport properties of these materials together with that of the polycrystalline antimony telluride and bismuth antimony telluride compositions will be reported elsewhere.

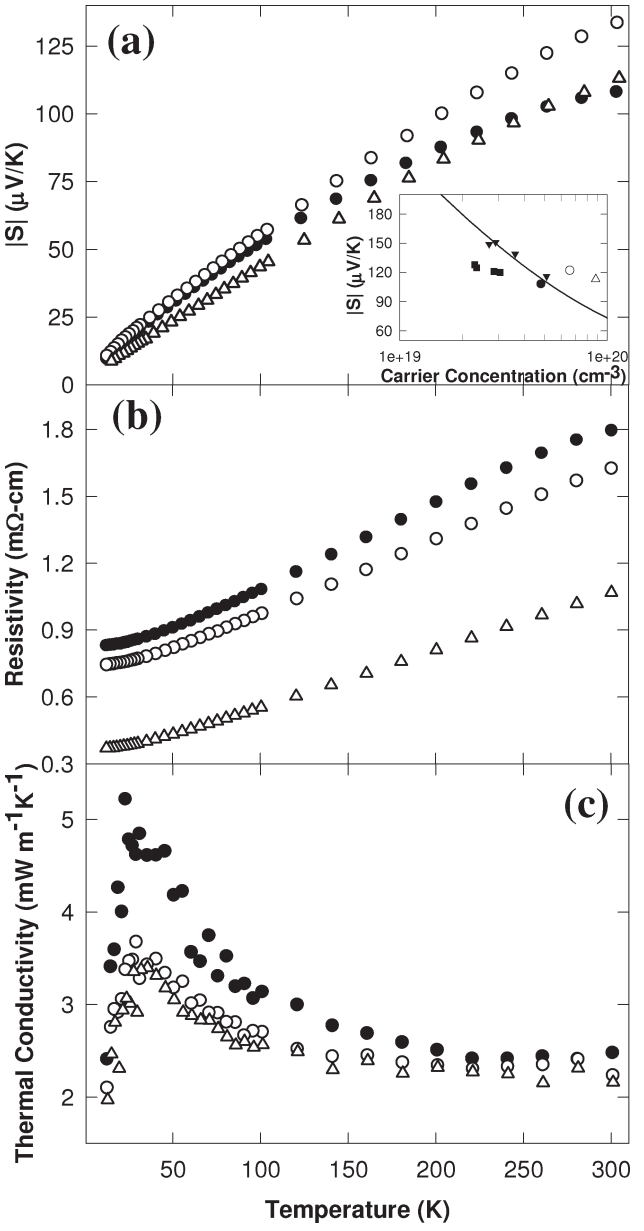

Figure 6. (a) Absolute Seebeck coefficient, $|S|$, (b) resistivity, ρ, and (c) thermal conductivity, κ, as a function of temperature for undoped (BT, ●) and Se doped (BT-1, ○; BT-2, Δ) polycrystalline Bi_2Te_3 nanocomposites. Room temperature $|S|$ versus n for the three specimens in comparison to bulk polycrystalline Bi_2Te_3 (▼ Kim et al.;[47] ■ Zhao et al.[48]) is shown in the inset of (a). The solid line represents the theoretical bulk relation, as described in the text.

4. Conclusion

Undoped and Se doped binary Bi_2Te_3 and Sb_2Te_3, as well as Se doped ternary $Bi_{0.5}Sb_{1.5}Te_3$, nanocrystals were prepared by a facile glycol-mediated nontemplated solvothermal process yielding high purity nanocrystals in large quantities. Both undoped and Se doped Bi_2Te_3 and $Bi_{0.5}Sb_{1.5}Te_3$ nanocrystals are spherical in shape, while Sb_2Te_3 are flake-like. The use of ethylene glycol as the solvent and Na_2TeO_3 as the Te source helps control the reaction rate and the growth rate of the nanocrystals thus allowing for a direct, scalable, and nontoxic bottom-up synthesis route for the densification and optimization of nanoscale thermoelectric materials. Densification via SPS results in nonagglomerated, dense polycrystalline alloys that contain nanoscale grains that are of interest for thermoelectric applications. This process can be extended to synthesize other telluride and selenide alloy nanocrystals.

Acknowledgment. This work was supported by the U.S. Army Medical Research and Material Command under Grant No. W81XWH-07-1-0708 and the National Science Foundation under Grant No. CMMI-0927637. The full description of the procedures used in this paper requires the identification of certain commercial products and their suppliers. The inclusion of such information should in no way be construed as indicating that such products or suppliers are endorsed by NIST or are recommended by NIST or that they are necessarily the best materials, instruments, software, or suppliers for the purposes described.

References

(1) Hicks, L. D.; Dresselhaus, M. S. *Phys. Rev B* **1993**, *47*, 12727.
(2) Bell, L. E. *Science* **2008**, *321*, 1457.
(3) Dresselhaus, M. S.; Chen, G.; Tang, M. Y.; Yang, R.; Lee, H.; Wang, D.; Ren, Z.; Fleurial, J. −P.; Gogna, P. *Adv. Mater.* **2007**, *19*, 1043.
(4) Heremans, J. P.; Thrush, C. M.; Morelli, D. T. *J. Appl. Phys.* **2005**, *98*, 063703.
(5) Kanatzidis, M. G. *Chem. Mater.* **2010**, *22*, 869.
(6) Nolas, G. S.; Sharp, J Goldsmid, H. J. *Thermoelectrics: Basic Principles and New Materials Developments*; Springer: New York, NY, 2001.
(7) Martin, J.; Nolas, G. S.; Zhang, W.; Chen, L. *Appl. Phys. Lett.* **2007**, *99*, 222112.
(8) Martin, J.; Wang, L.; Chen, L.; Nolas, G. S. *Phys. Rev. B* **2009**, *79*, 115311.
(9) Popescu, A.; Woods, L. M.; Martin, J.; Nolas, G. S. *Phy. Rev. B* **2009**, *79*, 205302.
(10) Venkatasubramanian, R.; Siivola, E.; Colpitts, T.; O'Quinn, B. *Nature* **2001**, *413*, 597.
(11) Zide, J. M. O.; Vashaee, D.; Bian, Z. X.; Zeng, G.; Bowers, J. E.; Shakouri, A.; Gossard, A. C. *Phys. Rev. B* **2006**, *74*, 205335.
(12) Kong, T.; Cronin, S. B.; Dresselhaus, M. S. *Appl. Phys. Lett.* **2000**, *77*, 1490.
(13) Zhao, Y.; Dyck, J. S.; Hernandez, B. M.; Burda, C. *J. Am. Chem. Soc.* **2010**, *132*, 4982.
(14) Ravich, Y. I. *CRC Handbook of Thermoelectrics*; Rowe, D. M., Ed.; CRC Press: New York, 1995; p 67.
(15) Goldsmid, H. J. *Thermoelectric Refrigeration*; Plenum: NewYork, 1964.
(16) Yim, W. M.; Rosi, F. D. *Solid-State Electron.* **1972**, *15*, 1121.
(17) Madelung, O.; Rössler, U.; Schulz, M. *Landolt-Börnstein - Group III Condensed Matter Numerical Data and Functional Relationships in Science and Technology, Non-Tetrahedrally Bonded Elements and Binary Compounds I*; Springer-Verlag: New York, 1998, 41, 1−4.
(18) Smith, M. J.; Knight, R. J.; Spencer, C. W. *J. Appl. Phys.* **1962**, *33*, 2186.
(19) Poudel, B.; Hao, Q.; Ma, Y.; Lan, Y. C.; Minnich, A.; Yu, B.; Yan, X.; Wang, D. Z.; Muto, A.; Vashaee, D.; Chen, X. Y.; Liu, J. M.; Dresselhaus, M. S.; Chen, G.; Ren, Z. F. *Science* **2008**, *320*, 634.
(20) Ma, Y.; Hao, Q.; Poudel, B.; Lan, Y. C.; Yu, B.; Wang, D. Z.; Chen, G.; Ren, Z. F. *Nano Lett.* **2008**, *8*, 2580.
(21) Lan, Y.; Poudel, B.; Ma, Y.; Wang, D.; Dresselhaus, M. S.; Chen, G.; Ren, Z. *Nano Lett.* **2009**, *9*, 1419.
(22) M -Gonzalez, M.; Prieto, A. L.; Gronsky, R.; Sands, T.; Stacy, A. M. *Adv. Mater.* **2003**, *15*, 1003.
(23) Yoo, B.; Xiao, F.; Bozhilov, K. N.; Herman, J.; Ryan, M. A.; Myung, N. V. *Adv. Mater.* **2007**, *19*, 296.
(24) Xie, W.; Tang, X.; Yan, Y.; Zhang, Q.; Tritt, T. M. *Appl. Phys. Lett.* **2009**, *94*, 102111.
(25) Ritter, J. J.; Maruthamuthu, P. *Inorg. Chem.* **1997**, *36*, 260.
(26) Purkayastha, A.; Kim, S.; Gandhi, D. D.; Ganesan, P. G.; Tasciuc, T. B.; Ramanath, G. *Adv. Mater.* **2006**, *18*, 2958.
(27) Zhao, Y.; Burda, C. *ACS Appl. Mater. Inter.* **2009**, *1*, 1259.
(28) Dirmyer, M. R.; Martin, J.; Nolas, G. S.; Sen, A.; Badding, J. V. *Small* **2009**, *5*, 933.
(29) Scheele, M.; Oeschler, N.; Meier, K.; Kornowski, A.; Klinke, C.; Weller, H. *Adv. Funct. Mater.* **2009**, *19*, 3476.

(30) Foos, E. E.; Stroud, R. M.; Berry, A. D. *Nano Lett*. **2001**, *1*, 693.
(31) Lu, W.; Ding, Y.; Chen, Y.; Wang, Z. L.; Fang, J. *J. Am. Chem. Soc*. **2005**, *127*, 10112.
(32) Shi, S.; Cao, M.; Hu, C. *Crys. Growth Des*. **2009**, *9*, 2057.
(33) Shi, W.; Yu, J.; Wang, H.; Zhang, H. *J. Am. Chem. Soc*. **2006**, *128*, 16490.
(34) Shi, W.; Zhou, L.; Song, S.; Yang, J.; Zhang, H. *Adv. Mater*. **2008**, *20*, 1892.
(35) Wang, W.; Poudel, B.; Yang, J.; Wang, D. Z.; Ren, Z. F. *J. Am. Chem. Soc*. **2005**, *127*, 13792.
(36) Wang, W.; Yan, X.; Poudel, B.; Ma, Y.; Hao, Q.; Yang, J.; Chen, G.; Ren, Z. *J. Nanosci. Nanotechnol*. **2008**, *8*, 452.
(37) Zhang, G.; Wang, W.; Lu, X.; Li, X. *Crys. Growth Des*. **2009**, *9*, 145.
(38) Zhou, B.; Ji, Y.; Yang, Y.-F.; Li, X.-H.; Zhu, J.-J. *Crys. Growth Des*. **2008**, *8*, 4394.
(39) Scherrer, P. *Nachr. Göttingen* **1918**, *2*, 98.
(40) Masala, O.; Seshadri, R. *Annu. Rev. Mater. Res*. **2004**, *34*, 41.
(41) Ye, J.; Qi, L. *J. Mater. Sci. Technol*. **2008**, *24*, 529.
(42) Lu, W. G.; Ding, Y.; Chen, Y. X.; Wang, Z. L.; Fang, J. Y. *J. Am. Chem. Soc*. **2005**, *127*, 10112.
(43) Ozin, G.; Arsenault, A. *Nanochemistry, A Chemical Approach to Nanomaterials*; Royal Society of Chemistry Publishing: Cambridge, 2005.
(44) Martin, J.; Nolas, G. S.; Wang, H.; Yang, J. *J. Appl. Phys*. **2007**, *102*, 103719.
(45) Ioffe, A. F. *Physics of Semiconductors*; Academic: New York, 1960.
(46) Madelung, O.; Schulz, M.; Weiss, H. *Landolt-Börnstein−Physics of Non-Tetrahedrally Bonded Binary Compounds II, New Series, Group-III*; Springer-Verlag: New York, 1983; p 17.
(47) Kim, D. H.; Mitani, T. *J. Alloys Compd*. **2005**, *399*, 14.
(48) Zhao, L. D.; Zhang, B.-P.; Liu, W. S.; Zhang, H. L.; Li, J.-F. *J. Alloys Compd*. **2009**, *467*, 91.